RSC Advances

PAPER

View Article Online
View Journal | View Issue

Cite this: *RSC Adv.*, 2025, **15**, 29703

Implementing a solid-state synthesis route to tune the functional properties of $NaCdP_3O_9$ metaphosphate: optical characteristics, ionic conductivity, and dielectric behavior

M. Karray,[a] I. Garoui,[a] M. Akermi,*[b] R. Djebali,[c] A. Oueslati*[a] and M. Gargouri[a]

Received 11th June 2025
Accepted 6th August 2025

DOI: 10.1039/d5ra04138d

rsc.li/rsc-advances

An in-depth analysis of $NaCdP_3O_9$ was performed, exploring its structural framework, vibrational dynamics, optical absorption, and electrical behavior. The compound was synthesized using a low-cost, conventional solid-state route, resulting in a well-defined orthorhombic crystal structure assigned to the $P2_12_12_1$ space group. Optical studies identified a direct energy band gap of 3.88 eV. Dielectric measurements revealed pronounced dependencies on both frequency and temperature, with high dielectric permittivity values at low frequencies ($\varepsilon' \approx 1.19 \times 10^3$). Charge transport is primarily facilitated through a polaron hopping mechanism. DC conductivity followed Arrhenius behavior, indicating thermally activated motion of sodium ions with an activation energy of 0.45 eV. Additionally, AC conductivity and dielectric analyses support a conduction process involving localized charge carriers surmounting correlated energy barriers, in agreement with the correlated barrier hopping (CBH) model. This study underscores the synergy between solid-state synthetic strategies and functional property optimization, positioning metaphosphate materials as strong candidates for future sustainable electronic technologies.

1. Introduction

The search for new Na/Li-based conductors has gained significant momentum in recent years due to their unique structural features, semiconducting behavior, and favorable electrochemical properties.[1–3] Recently, with the increasing price volatility of lithium resources and the emergence of sodium-ion batteries, solid-state sodium batteries have garnered considerable attention.[2,4] These materials hold great potential for applications in portable electronics and electric vehicles, where the demand for high energy density is rapidly increasing.[5,6] Among the various families of sodium-based materials, transition metal-containing monophosphates and diphosphates have attracted interest due to their structural diversity and stability under different processing conditions.[7–10] In particular, phosphate-based materials have been extensively investigated due to their robust crystal frameworks, chemical stability, and favorable thermal properties. Transition metal phosphates exhibit diverse polyhedral connectivity (*e.g.*, corner-sharing or edge-sharing configurations), which facilitates fast ion transport.[11,12] The substitution of smaller O^{2-} ions with bulkier polyanions such as $(PO_4)_3^-$ or $(P_2O_7)^{3-}$ in open three-dimensional frameworks enhances structural stability and broadens diffusion pathways for improved ion migration.[13,14]

Phosphate-based dielectric ceramics have also gained significant attention due to their excellent dielectric properties, including high dielectric constants, superior quality factors, and low synthesis temperatures. Several studies have investigated $NaMP_3O_9$ compounds, where M = Fe, Mn, Co, Zn, or Mg.[7,15–18] However, $NaCdP_3O_9$ remains relatively unexplored, with prior research primarily focused on its crystal structure.[19] These compounds crystallize in an orthorhombic structure (space group $P2_12_12_1$), where PO_4 tetrahedra form infinite, heavily bent $(PO_3)^-$ chains composed of 24 tetrahedra, while Na and Cd cations are octahedrally coordinated by terminal oxygen atoms of the PO_4 tetrahedra. Expanding on previous studies, this work aims to deepen the understanding of the optical properties, dielectric behavior, and conduction mechanisms of $NaCdP_3O_9$, with a particular focus on its microscopic-scale transport phenomena.

To date, only a few metal metaphosphate compounds, such as $NaCoP_3O_9$ (ref. 15) and $NaFeP_3O_9$,[20] have been studied in detail. These investigations have revealed their unique physicochemical properties and potential as cathode materials for rechargeable batteries. However, their electrical properties and ion conduction mechanisms remain largely unexplored, leaving room for further research to fully understand their functional

[a]*Laboratory of Spectroscopic and Optical Characterization of Materials (LaSCOM), Faculty of Sciences, University of Sfax, B. P. 1171, 3000 Sfax, Tunisia. E-mail: oueslatiabderrazek@yahoo.fr*

[b]*Department of Physics Sciences, College of Science, Jazan University, P.O. Box. 114, Jazan 45142, Kingdom of Saudi Arabia. E-mail: makermi@jazanu.edu.sa*

[c]*UR: Modeling, Optimization and Augmented Engineering, ISLAI Béja, University of Jendouba, Béja 9000, Tunisia*

capabilities. Despite their promising electrochemical performance, the ionic conductivity of metal metaphosphates remains uncharacterized. Consequently, a comprehensive structural and electrical study of these materials is essential to elucidate their ionic transport mechanisms and assess their potential technological applications.

This study presents the synthesis and comprehensive characterization structural, optical, and electrical of the sodium-based metal metaphosphate $NaCdP_3O_9$. The compound was successfully prepared *via* a straightforward solid-state route, and its crystalline structure was verified through powder X-ray diffraction analysis. The optical band gap was estimated using UV-visible spectroscopy. Impedance spectroscopy, recognized as a powerful technique for probing dielectric behavior, was employed to investigate the material's response as a function of both temperature and frequency. This analysis enabled an in-depth evaluation of various key properties, including charge carrier dynamics, conduction mechanisms, and dielectric permittivity. The temperature- and frequency-dependent studies provided valuable insights into the behavior of localized charge carriers within the system. Overall, this work not only deepens the understanding of $NaCdP_3O_9$ but also makes a meaningful contribution to the growing body of research on metaphosphate materials, highlighting their potential in a wide range of advanced technological applications.

2. Materials and methods

2.1. Preparation

The $NaCdP_3O_9$ metaphosphate compound was successfully synthesized using the solid-state reaction method. The precursor oxides and salts cadmium oxide (CdO), sodium carbonate (Na_2CO_3), and ammonium dihydrogen phosphate ($NH_4H_2PO_4$) were accurately weighed and thoroughly mixed in stoichiometric proportions as follows:

$$2CdO + Na_2CO_3 + 6NH_4H_2PO_4 = 2NaCdP_3O_9 + 6NH_3 + 9H_2O + CO_2$$

To synthesize 2 g of $NaCdP_3O_9$, the precursor materials sodium carbonate (Na_2CO_3, 0.284 g), cadmium oxide (CdO, 0.689 g), and ammonium dihydrogen phosphate ($NH_4H_2PO_4$, 1.853 g) were precisely weighed in stoichiometric proportions. The methodology involved several steps, as depicted in Fig. 1. The reagents were manually ground in an agate mortar for 4 hours in air to reduce particle size, improve homogeneity, and enhance reactivity. Achieving a uniform mixture is essential for accelerating reaction kinetics.

The finely ground powder was then placed in a ceramic crucible and subjected to an initial calcination at 673 K for 8 hours in a programmable electric furnace, with a controlled heating rate of 5 K per minute. This preliminary heat treatment aimed to eliminate volatile components such as NH_3, CO_2 and H_2O, facilitating the formation of $NaCdP_3O_9$. Following calcination, the powder was reweighed and manually reground for an additional 8 hours to ensure uniformity. Before high-temperature treatment, the powder was compressed into pellets with an 8 mm diameter using uniaxial pressure, promoting the reaction. Finally, the obtained green pellets were sintered at 873 K for 4 hours in an air atmosphere, a process that enhances diffusion, densification, and structural consolidation.

2.2. Technical characterizations

X-ray diffraction (XRD) analysis was performed on the powdered sample at room temperature using a Bruker diffractometer with CuKα radiation ($\lambda = 1.5406$ Å), covering a 2θ range of 10° to 70°. The infrared spectrum IR was acquired in the wave number range 400–1300 cm^{-1} using an FTIR-100 PerkinElmer spectrophotometer. The optical absorption spectrum of sample was measured at room temperature in the wavelength range of 200–

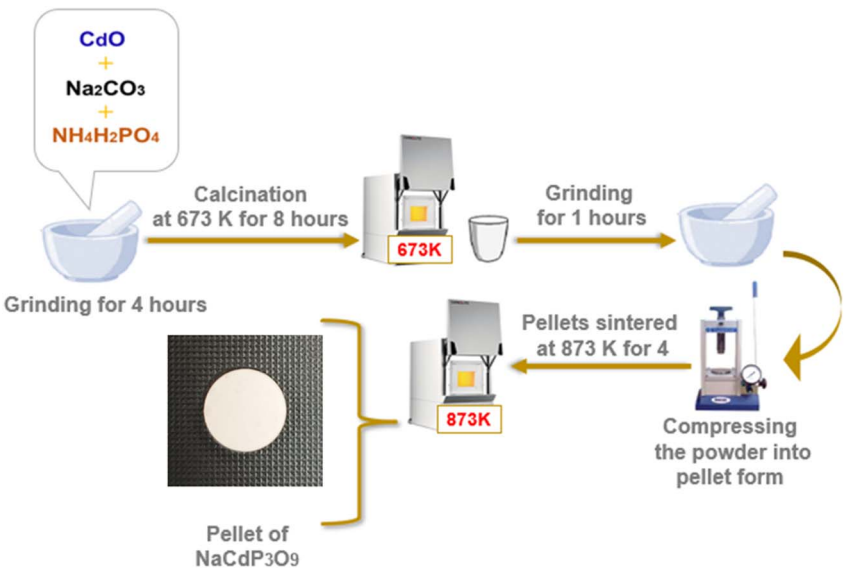

Fig. 1 The synthesis steps for $NaCdP_3O_9$ *via* the solid-state method.

800 nm using a UV-vis spectrophotometer (SHIMADZU 3101PC).

Impedance spectroscopy was utilized to investigate the electrical and dielectric properties of $NaCdP_3O_9$. The dielectric material was shaped into a disc-shaped capacitor with an 8 mm diameter and 1 mm thickness. To ensure optimal electrical contact, both surfaces of the pellets were coated with a thin layer of silver. The sample was then placed in a cryostat, allowing precise temperature control within the 473–673 K range. For accurate measurements, the sample was positioned in a temperature-controlled chamber, where continuous regulation minimized temperature fluctuations. Platinum electrodes were employed to provide stable and reproducible electrical contact. Impedance measurements were conducted at standard atmospheric pressure using a Solartron 1260 dielectric spectrometer, applying a 1 V signal across a broad frequency range (20 to 4×10^6 Hz).

3. Results and discussion

3.1. X-ray diffraction examination

To verify the purity and crystallinity of the metaphosphate $NaCdP_3O_9$ sample, X-ray diffraction (XRD) analysis was performed using a diffractometer equipped with a copper anticathode ($\lambda_{CuK\alpha_1} = 1.5406$ Å). The XRD pattern, recorded at room temperature over the 2θ range of 10° to 70°, is presented in Fig. 2(a). The structural refinement of the $NaCdP_3O_9$ compound was carried out using the FullProf software,[21] considering literature data from M. M. T. Averbuch-Pouchot and A. Durif,[19] as well as information on isostructural compounds $NaXP_3O_9$ (X = Co, Fe, and Mn).[15,16,22] The diffraction patterns exhibit distinct peaks characteristic of an orthorhombic structure, with primary reflections indexed to the $P2_12_12_1$ space group.

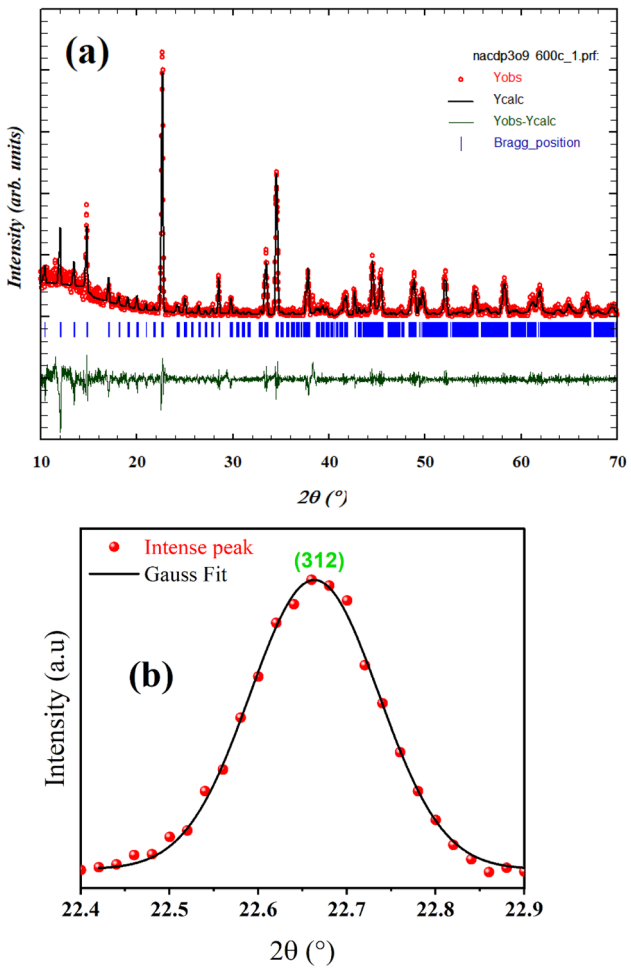

Fig. 2 (a) X-ray diffraction (XRD) of $NaCdP_3O_9$ at room temperature. (b) The Debye–Scherrer plot for $NaCdP_3O_9$ compound.

In Fig. 2(a), the Bragg positions, marked by vertical blue bars, align well with the orthorhombic phase, confirming phase purity. The lower blue curve illustrates the difference between the observed and calculated diffraction patterns. The refined structural parameters are summarized in Table 1. The goodness-of-fit value ($\chi^2 \approx 1.96$) indicates an excellent agreement between the experimental and calculated profiles, further validating the accuracy of the refinement. When comparing the unit cell parameters of the studied $NaCdP_3O_9$ compound with those of $NaCoP_3O_9$,[15] it is evident that the unit cell of $NaCdP_3O_9$ is larger. This expansion aligns well with the difference in ionic radii of the metal cations in octahedral coordination, where $R(Co^{2+}) = 0.745$ Å and $R(Cd^{2+}) = 0.95$ Å, confirming the expected structural trend.

The XRD diffractogram of the sample reveals that the most intense peak corresponds to the (312) plane, with a diffraction angle (2θ) of 22.68° (see Fig. 2(b)). The average crystallite size of the $NaCdP_3O_9$ sample was estimated using this dominant peak and calculated based on the Debye–Scherrer equation:[23]

$$D_{sc} = \frac{0.9\lambda}{\beta \cos(\theta)} \quad (1)$$

In this equation, λ represents the X-ray wavelength (1.54056 Å), θ is the diffraction angle, and β denotes the full width at half maximum (FWHM) of the peak. Based on this calculation, the average crystallite size was found to be 59.48 nm.

Table 1 Refined structural parameters of the $NaCdP_3O_9$ compound at room temperature

Sample	$NaCdP_3O_9$
Structure	Orthorhombic
Space group	$P2_12_12_1$
D_{SC} (nm)	59.48
Unit cell parameter	
a (Å)	14.628896
b (Å)	14.657402
c (Å)	14.741147
V (Å^3)	3160.820465
Agreement factors	
R_p (%)	42.5
R_{exp}(%)	36.06
R_{wp} (%)	50.5
R_F (%)	2.234
R_{Bragg} (%)	2.560
χ^2	1.96

3.2. Band gap energy and vibrational characteristics

3.2.1. Vibrational mode analysis. Infrared spectroscopy was utilized to gain deeper insight into the vibrational behavior of the $NaCdP_3O_9$ compound. As shown in Fig. 3, the FTIR spectrum displays multiple absorption bands characteristic of the vibrational modes of linear polyphosphate groups. These characteristic bands provide insight into the bonding environment and structural framework of the phosphate network. Table 2 summarizes the observed spectral frequencies along with their corresponding vibrational assignments. The attributions of these bands were made by referring to previously published data,[24–26] following a sequence of metaphosphate vibrations ranked by declining frequency, which are typically interpreted by dividing the spectrum into two distinct regions: above and below 600 cm^{-1}.

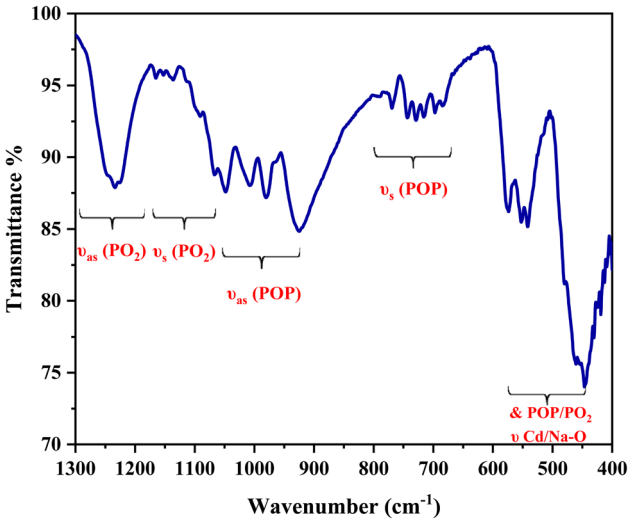

Fig. 3 Infrared spectrum analysis of $NaCdP_3O_9$ at room temperature.

In the high-frequency region (>600 cm^{-1}), the absorption bands observed between 1290–1220 cm^{-1} and 1170–1060 cm^{-1} correspond to the asymmetric and symmetric stretching vibrations of the terminal PO_2 groups, respectively.

Other bands appearing in the range of 1050–900 cm^{-1} and 850 and 600 cm^{-1} are assigned to asymmetric and symmetric stretching modes of P–O–P bridges. These attributions align well with the typical vibrational behavior observed in metaphosphate-based compounds, including species like pyrophosphates ($P_2O_7^{4-}$), triphosphates ($P_3O_{10}^{5-}$), and various other linear or cyclic phosphate anions. The pronounced absorption band near 1270 cm^{-1} is particularly significant, as it corresponds to the asymmetric stretching vibrations of the $(PO_3)^{1-}$ chain units, which are central to the structural framework of metaphosphate compounds.

In the lower frequency region (<600 cm^{-1}), the absorption features become more complex and are mainly related to bending vibrations of the PO_4 tetrahedra as well as to metal–oxygen interactions, such as Na–O and Cd–O bonds. These observations confirm that $NaCdP_3O_9$ consists of a connected phosphate network composed of both terminal and bridging phosphate units, consistent with its structural classification as a linear metaphosphate compound.

3.2.2. Optical properties and band gap determination. UV/vis spectroscopy is widely used to perform quantitative optical analysis, particularly in the study of ceramic materials. This

Table 2 IR vibrational frequencies (cm^{-1}) for $NaCdP_3O_9$ compound

Wave number (cm^{-1})	Assignments
1234	$\upsilon_{as}(PO_2)$
1165	
1153	
1135	$\upsilon_s(PO_2)$
1114	
1092	
1066	
1048	
1006	υ_{as} (POP)
980	
925	
768	
729	υ_s (POP)
716	
696	
682	
573	
552	
541	P–O & O–P–O bend
479	
475	
446	

technique measures the amount of light absorbed or transmitted in the ultraviolet and visible regions of the electromagnetic spectrum. One of the key outcomes of this analysis is the determination of the bandgap energy the minimum energy required to excite an electron from the valence band to the conduction band. Knowing the bandgap is essential for assessing a material's ability to absorb and emit light, which is critical for its application in photovoltaics, light-emitting devices, and photocatalysis.[27,28]

The optical absorption spectrum of $NaCdP_3O_9$ was recorded in the UV-visible range to investigate its electronic transitions, optical band gap and Urbach energy. As shown in Fig. 4(a), the material exhibits two prominent absorption peaks centered at 258 nm and 292 nm, which are typically attributed to charge-transfer transitions involving oxygen and metal cations ($O^{2-} \rightarrow Cd^{2+}/P^{5+}$), a characteristic commonly observed in phosphate-based compounds.[29–31]

The optical band gap energy (E_g) of $NaCdP_3O_9$ was determined by locating the inflection point on the high-energy side of the $dA/d\lambda$ curve. Applying the Marotti equation, which links photon energy to wavelength, E (eV) = 1239.8/(nm),[32] the band gap was calculated to be 3.97 eV, corresponding to a wavelength of 312 nm. To determine the nature of the optical band gap whether direct or indirect the Tauc method[33] was employed for a precise evaluation of E_g.

$$(\alpha h\nu)^n = A(h\nu - E_g) \quad (2)$$

In this equation, $h\nu$ represents photon energy, α_0 denotes the optical constant, and n takes a value of 1/2 for direct transitions or 2 for indirect transitions.

Fig. 4(b) presents the relationship between $(\alpha h\nu)^2$ and $(\alpha h\nu)^{1/2}$ as a function of photon energy ($h\nu$). The analysis of this plot revealed a direct optical band gap (E_{gd}) of 3.88 eV and an indirect band gap (E_{gi}) of 3.68 eV. To verify the transition type (direct/indirect), eqn (2) was reformulated to yield the following expression:

$$\ln(\alpha h\nu) = \ln(\alpha_0) + n\ln(h\nu - E_g) \quad (3)$$

Inset of Fig. 4(b) illustrates the relationship between $\ln(\alpha h\nu)$ and $\ln(h\nu - E_g)$ for $NaCdP_3O_9$, displaying a linear trend. The slope-derived power factor ($n = 0.3$) confirms direct semiconductor behavior, consistent with results from the Marotti method. These values are characteristic of wide optical band gap semiconductors, highlighting their suitability for optoelectronic applications.[34]

To investigate the material's structural disorder, the Urbach energy (E_u) was calculated using the following expression:[35]

$$\ln(\alpha) = \ln(\alpha_0) + \frac{h\nu}{E_u} \quad (4)$$

The Urbach energy ($E_{(u)}$) determined for $NaCdP_3O_9$, estimated to be around 0.27 eV from the linear region of the $\ln(\alpha)$ *versus* photon energy ($h\nu$) plot Fig. 4(c), suggests a low density of localized states and a relatively ordered crystal structure.

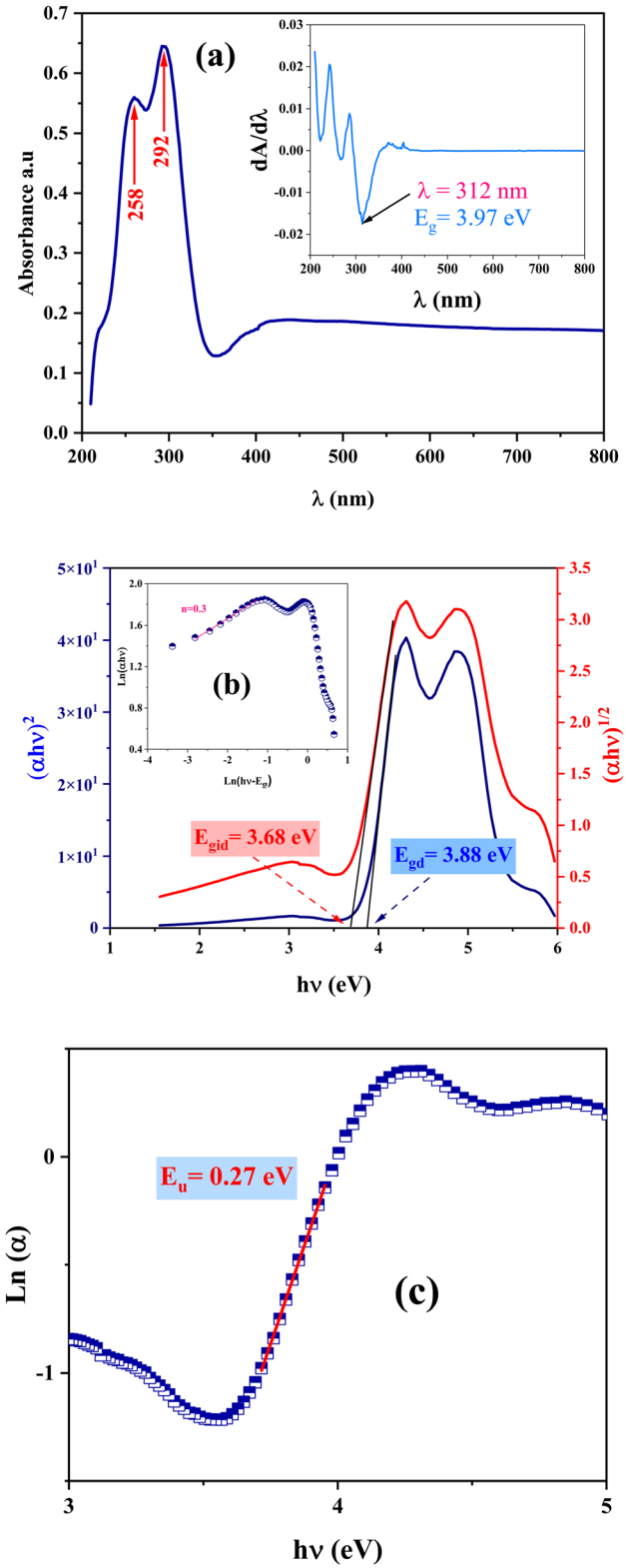

Fig. 4 (a) The UV-vis absorbance spectrum and $dA/d\lambda$ as a function of λ (inset) for the phosphors $NaCdP_3O_9$. (b) Variation of $(\alpha h\nu)^2$ and $(\alpha h\nu)^{1/2}$ plots *vs.* $h\nu$ for band gap of $NaCdP_3O_9$ and variation of $\ln(\alpha h\upsilon)$ against $\ln(h\upsilon - E_g)$ determination (inset). (c) Determining the Urbach energy.

The Urbach energy (E_u) can also be estimated using the following relation:

$$E_u = \frac{k_B T}{\sigma} \quad (5)$$

where k_B is the Boltzmann constant, T is the absolute temperature (typically taken as 300 K), and s is a parameter that quantifies how rapidly the absorption edge broadens as a result of electron–phonon interactions within the band gap.[36]

The parameter σ was found to be around 0.01. This coefficient, which indicates the intensity of the electron–phonon interaction (E_{e-ph}), can be described using the following expression:[37]

$$E_{e-ph} = \frac{2}{3\sigma} \quad (6)$$

The calculated electron–phonon interaction energy (E_{e-ph}) is about 6.95 eV. This interaction characterizes the coupling between charge carriers and lattice vibrations (phonons), which significantly influences key material properties such as electrical resistivity, thermal conductivity, and superconducting behavior.

$NaCdP_3O_9$ exhibits excellent optical properties, with a wide band gap of 3.88 eV, a sharp UV cut-off at 252 nm, broad transparency from 292 to 800 nm, and a low Urbach energy of 0.27 eV, indicating high structural order. These characteristics make it a promising material for UV-transparent windows, optical coatings, and photonic devices operating in the UV-visible range, especially where thermal and optical stability are critical.

3.3. Impedance evolution across frequency and temperature

Following structural, vibrational, and optical characterization, the electrical properties were examined through Complex Impedance Spectroscopy (CIS). This technique establishes a connection between theoretical circuit elements and the actual electrical behavior of the system, offering valuable insights into microstructural features such as grains, grain boundaries, and electrode interfaces. Additionally, CIS enables the determination of essential parameters, by employing complex impedance formalism (Z^*) across different frequencies and temperatures. By resolving the real (Z') and imaginary (Z'') components of the complex impedance (Z^*), CIS provides a comprehensive and precise depiction of the material's electrical characteristics.[38]

$$Z^* = Z'(\omega) - jZ''(\omega) \quad (7)$$

To gain a deeper understanding of the relaxation and conduction mechanisms within the material, impedance data is analyzed using the Cole–Cole representation, which is a complex plane plot of the real $Z'(\omega)$ and imaginary $Z''(\omega)$ components of the electrical impedance, commonly referred to as the Nyquist plot. This approach involves simulating experimental data using an idealized circuit model composed of discrete electrical branches, where the material's electrical behavior is described through equivalent RC-parallel connections. By employing this method, the contributions of different regions within the material can be distinguished, enabling a comprehensive assessment of its intrinsic electrical response.

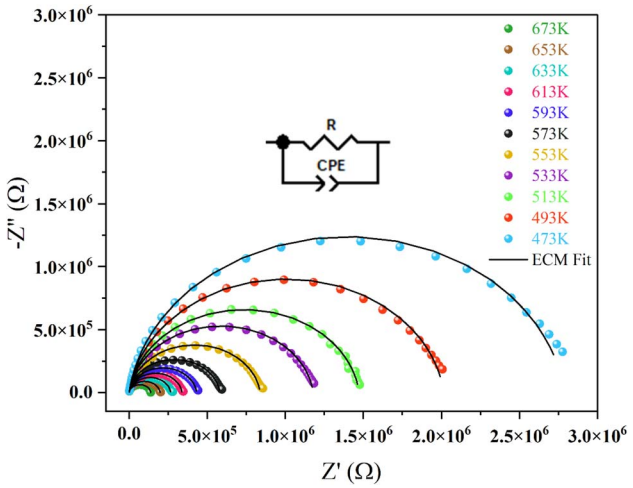

Fig. 5 Nyquist plot of $NaCdP_3O_9$ compound, at different temperatures with equivalent circuit model in the inset.

The Nyquist plots for the $NaCdP_3O_9$ sample, recorded over a temperature range of 473–673 K in 20 K increments, are presented in Fig. 5. In these plots, experimental data points are represented by symbols, while the solid lines correspond to the fitted curves derived from the equivalent circuit model. The impedance spectra of $NaCdP_3O_9$ exhibit a single, depressed semicircular arc at all examined temperatures, indicating that the electrical response is predominantly governed by the bulk properties of the material. Consequently, the arcs observed in the Cole–Cole plots primarily represent the bulk behavior of the sample.[39]

In the Nyquist representation, the displacement of semicircle centers below the real impedance Z' axis indicates a deviation from ideal Debye-type relaxation,[40] suggesting the presence of a constant phase element (CPE) in the equivalent circuit model. Typically, a CPE is characterized by two parameters, CPE-T (Q) and CPE-P (α), and is mathematically defined as:

$$Z = \frac{1}{[(\text{CPE-T})(j\omega)]^{\text{CPE-P}}} \quad (8)$$

Here, CPE-T is expressed in units of capacitance, while (ω) is given in radians per second. The exponent CPE-P takes values of 1, 0, and 0.5, corresponding to capacitive, resistive, and Warburg components, respectively.[41] The diameters of the Nyquist plots represent the resistance values, which decrease with rising temperature. This trend indicates that as the temperature increases, charge carriers gain thermal activation, leading to a reduction in overall impedance and consequently enhancing electrical conduction.

The sample's impedance was further analyzed using equivalent circuit models (ECM) to gain deeper insights into its electrical behavior. The experimental data from the Nyquist plot

Table 3 Electrical values of the equivalent circuit parameters calculated for $NaCdP_3O_9$ compound at different temperatures

T (K)	R ($\times 10^5$ Ω)	CPE-T (Q) ($\times 10^{-11}$ F)	CPE-P (α)
673	1.3789	11	0.93791
653	1.9802	11.56	0.93412
633	2.6598	11.46	0.93449
613	3.3774	10.55	0.93996
593	4.3401	10.37	0.94088
573	5.8105	10.80	0.93798
553	8.3974	11.36	0.93541
533	11.778	11.66	0.93316
513	14.762	11.98	0.93079
493	20.311	12.37	0.92895
473	28.281	13.10	0.92422

was fitted using ZView software, with the optimal fit aligning with the (R//CPE) equivalent circuit configuration, as depicted in the inset of Fig. 5. In this model, (R) and CPE correspond to the bulk resistance and capacitance, respectively. The component values were extracted from ZView following the ECM fitting process.

The parameters derived from the equivalent circuit are presented in Table 3. Notably, the capacitance CPE-T is approximately 10^{-11} F. Furthermore, the resistance values (R) exhibit a decreasing trend with increasing temperature, which is consistent with the semiconducting behavior. The data in Table 3 also highlight the temperature-dependent variation of bulk resistance, clearly demonstrating a decline in resistance as temperature rises, thereby confirming the Negative Temperature Coefficient of Resistance (NTCR) characteristic.[42]

Fig. 6 presents the frequency-dependent variation of the real Z' and imaginary Z'' components of the complex impedance for $NaCdP_3O_9$ at different temperatures. In this study, the impedance spectra have been modeled using eqn (9) and (10) to accurately simulate the electrical response of the material.

$$Z'(\omega) = \frac{R\left(1 + RQ\omega^{\alpha_1}\cos\left(\frac{\alpha\pi}{2}\right)\right)}{\left(1 + RQ\omega^{\alpha}\cos\left(\frac{\alpha_1\pi}{2}\right)\right)^2 + \left(RQ\omega^{\alpha}\sin\left(\frac{\alpha\pi}{2}\right)\right)^2} \quad (9)$$

$$-Z''(\omega) = \frac{R^2\ Q\omega^{\alpha}\cos\left(\frac{\alpha\pi}{2}\right)}{\left(1 + RQ\omega^{\alpha}\cos\left(\frac{\alpha\pi}{2}\right)\right)^2 + \left(RQ\omega^{\alpha}\sin\left(\frac{\alpha\pi}{2}\right)\right)^2} \quad (10)$$

Fig. 6(a) illustrates the evolution of the real impedance Z' with angular frequency, highlighting three distinct regions that characterize the electrical response of $NaCdP_3O_9$ at varying temperatures and frequencies. In the low-frequency domain (Region I), Z' exhibits a temperature-dependent decrease across all frequencies. This behavior can be linked to charge carrier accumulation at grain boundaries,[43] a hallmark of DC conduction. In this regime, long-range charge transport is facilitated by an efficient hopping mechanism, enabling neighboring carriers to settle into equilibrium positions.[44,45] As the system transitions into the intermediate-frequency range (Region II),

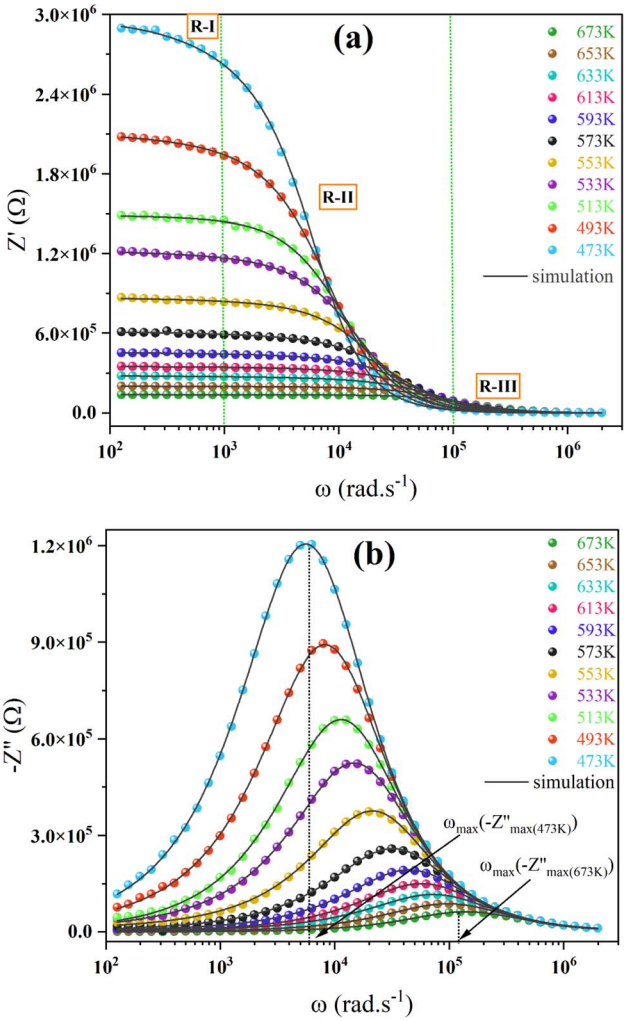

Fig. 6 (a) Variation of real part of the impedance with angular frequency at various temperatures for $NaCdP_3O_9$. (b) Variation of imaginary part of the impedance with angular frequency at various temperatures for $NaCdP_3O_9$.

a combined effect of increasing temperature and frequency enhances charge carrier mobility, leading to a continuous reduction in Z' and, consequently, an increase in AC conductivity. Beyond 10^5 Hz (Region III), the impedance values tend to merge, becoming almost independent of temperature. This trend is associated with the dissipation of space charges. Additionally, as temperature rises, the conduction barrier gradually weakens, leading to a substantial drop in AC current resistance and further promoting electrical conduction.[46]

Fig. 6(b) presents the temperature-dependent evolution of the imaginary impedance (Z'') as a function of frequency for undoped $NaCdP_3O_9$ samples. Beyond a characteristic frequency (ω_r), the magnitude of (Z'') declines progressively, eventually becoming negligible at higher frequencies. The broadening of the peak beyond its maximum position becomes more pronounced with increasing temperature, indicating a distribution of relaxation times that aligns with the condition ($\omega_r \cdot \tau = 1$).[47] The impedance spectra reveal a single peak at specific

frequencies, commonly referred to as relaxation frequencies. This peak, observed within the (6×10^3–124×10^3) Hz range depending on temperature, is associated with bulk relaxation. A noticeable shift of the relaxation frequency toward higher values with increasing temperature suggests thermally activated charge carriers accumulating at grain boundary interfaces. This trend further reinforces the semiconducting behavior of the studied material.

3.4. Electrical conductivity analysis

Fig. 7(a) presents the frequency-dependent complex conductivity of $NaCdP_3O_9$ metaphosphate at various temperatures. In these cases, a plateau is observed at low frequencies, followed by a dispersion region at higher frequencies. The electrical behavior of these metaphosphate is significantly influenced by the hopping mechanism and grain activity. The frequency-dependent conductivity curves exhibit a characteristic change in slope at a specific frequency, known as the hopping frequency (ω_H), which varies with temperature.

The conductivity spectrum can be divided into two regions: below ω_H, the conductivity is dominated by DC conduction (σ_{dc}), while above ω_H, AC conduction (σ_{ac}) prevails.[48] Consequently, the total conductivity is expressed as $\sigma = \sigma_{dc} + \sigma_{ac}$. The increase in conductivity with frequency at all temperatures follows a thermally activated process, where the number of charge carriers increases with temperature. Materials containing smaller ionic radii typically exhibit higher AC conductivity due to enhanced ionic mobility and faster charge transport. Conversely, materials with larger ionic radii tend to have lower AC conductivity due to reduced ion mobility and slower charge transfer.

The frequency-dependent conductivity behavior is well described by Jonscher's power law, given by:[49]

$$\sigma(\omega, T) = \sigma_{dc}(T) + A\omega^{s(T)} \quad (11)$$

where "A" reflects the strength of polarizability, and the frequency exponent "s" ranges between $0 < s < 1$.[50] The value of "s" is influenced by interactions between mobile ions, which, in turn, affect AC conductivity, while DC conductivity remains independent of frequency.

Using this relation, the values of σ_{dc}, A, and (s) were determined and are presented in Table 4.

At 473 K, the DC conductivity was measured at 0.618×10^{-7} Ω cm^{-1}, increasing to 12.893×10^{-7} Ω cm^{-1} at 673 K. This significant rise in conductivity with temperature confirms the semiconductor nature of the studied compound, as it follows the typical thermally activated behavior of semiconducting materials. The variation of DC conductivity with temperature for $NaCdP_3O_9$ nanomaterial is interpreted using the Arrhenius equation:[51]

$$\sigma_{dc}(T) = \sigma_0 e^{-\frac{E_a}{K_B \times T}} \quad (12)$$

Here, E_a represents the activation energy, which is determined from the slope of the linear fit in the $\ln(\sigma_{dc} \times T)$ *versus* $1/K_B \times T$ plot, as depicted in Fig. 7(b). For the $NaCdP_3O_9$ compound, the

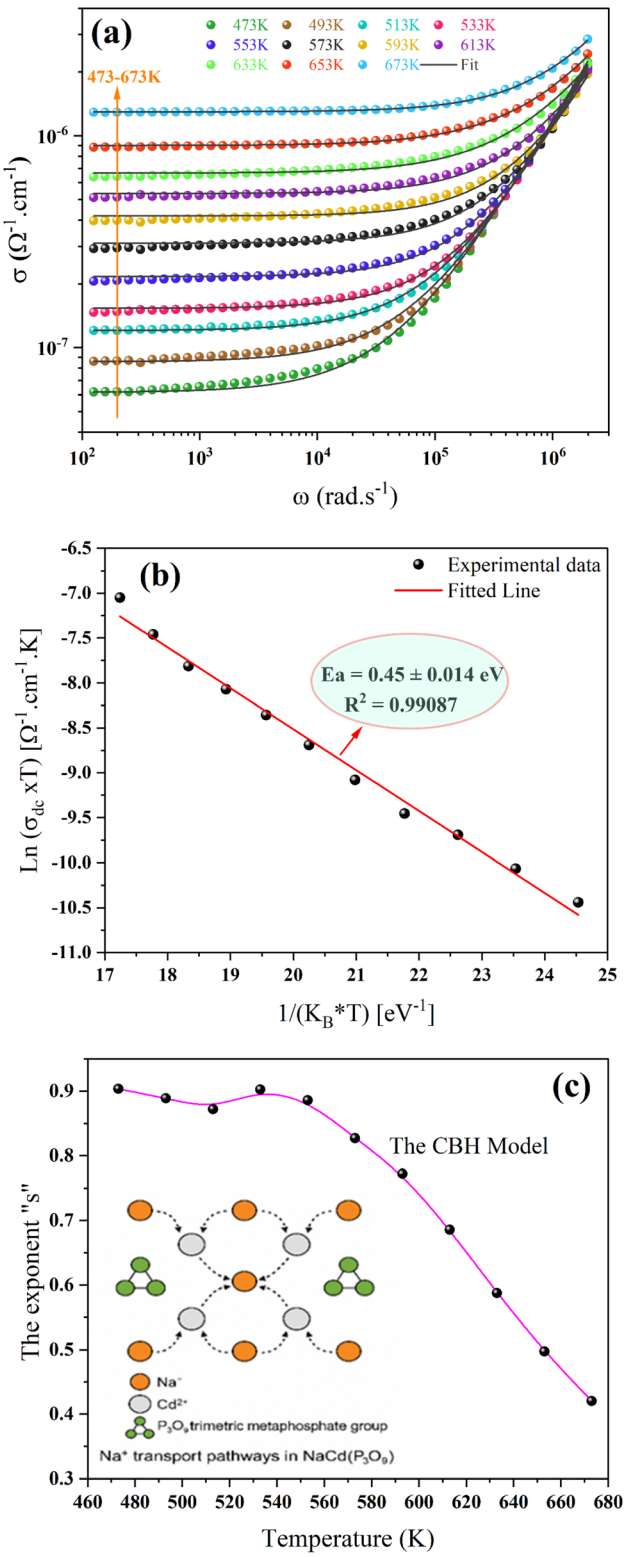

Fig. 7 (a) Frequency-dependent variation of the electrical conductivity of $NaCdP_3O_9$ at different temperatures. (b) Evolution of $\ln(\sigma_{dc} \times T)$ *versus* the reciprocal of temperature and the deduced activation energy value. (c) The temperature dependence of the frequency exponent "*s*".

Table 4 Jonscher law parameters for $NaCdP_3O_9$ at different temperatures

T (K)	σ_{dc} ($\times 10^{-7}$ Ω^{-1} cm^{-1})	A ($\times 10^{-12}$)	s
673	12.893	4.71802	0.42043
653	8.824	4.39247	0.49717
633	6.384	3.75241	0.58751
613	5.101	2.61389	0.68578
593	3.959	1.80829	0.77228
573	2.937	1.3356	0.82724
553	2.059	1.02844	0.88601
533	1.468	0.907046	0.90273
513	1.205	0.677136	0.87211
493	0.861	0.678976	0.88905
473	0.618	0.559423	0.90373

calculated activation energy is 0.45 ± 0.014 eV, aligning well with reported values for sodium-based dielectric materials such as $NaGaP_2O_7$,[52] $NaMnPO_4$,[12] and $NaCu_{0.2}Fe_{0.8-x}Mn_xO_2$ ($x = 0.4$, 0.5, 0.6, 0.7).[53] Charge carriers traverse the material by surmounting energy barriers. The 0.45 eV value corresponds to the energy necessary for charge carriers to hop between sites, facilitating electrical conduction.

The frequency exponent "*s*" provides insight into charge carrier-ion interactions and plays a crucial role in determining the conduction mechanism in $NaCdP_3O_9$. Its variation with temperature depends on the specific transport model:[54–57]

- In the Correlated Barrier Hopping (CBH) model, "*s*" exhibits an increasing trend as temperature rises.
- In the Non-Small Polaron Tunneling (NSPT) model, "*s*" decreases with increasing temperature.
- In the Overlapping Large Polaron Tunneling (OLPT) model, "*s*" initially declines, reaches a minimum, and then starts to rise again.
- When "*s*" remains nearly constant across different temperatures, it indicates that the material follows the Quantum Mechanical Tunneling (QMT) conduction mechanism.

Fig. 7(c) illustrates the temperature-dependent variation of the frequency exponent "*s*". Notably, "*s*" decreases as temperature increases within the studied range. This trend indicates that the conduction mechanism is well described by the Correlated Barrier Hopping (CBH) model, where charge transport occurs *via* polaron hopping across the Coulomb barrier separating two defect centers.[58]

The plausible sodium-ion (Na^+) conduction pathways within the crystal lattice of $NaCdP_3O_9$ is illustrated inset Fig. 7(c). The structure is composed of Na^+ ions, Cd^{2+} cations, and trimetric metaphosphate groups $P_3O_9^{3-}$, forming a three-dimensional network. The dashed arrows represent the expected hopping routes of Na^+ ions between energetically favorable sites. Due to the spatial arrangement of the $P_3O_9^{3-}$ units and Cd^{2+} centers, the sodium migration is not facilitated by direct edge-sharing polyhedral channels, but rather occurs through a series of discrete jumps. This geometry is consistent with a Correlated Barrier Hopping (CBH) conduction mechanism, where charge carriers hop between localized sites, overcoming potential barriers that are influenced by both the distance and the local structural environment.

The average hopping distance and the relatively open framework suggest moderate ion mobility, particularly at elevated temperatures. This is supported by the experimentally determined activation energy of 0.45 eV for $NaCdP_3O_9$, indicating that Na^+ migration is thermally activated. Similar conduction behavior has been reported in other polyphosphate-based materials, where the lack of continuous NaO_6 octahedral chains leads to constrained but directional ionic transport.[15]

As shown in Fig. 8, which illustrates a representative sodium-ion diffusion pathway in the $NaCdP_3O_9$ structure along the $[11\bar{1}]$ direction, the NaO_6 octahedra are widely spaced and connected through PO_4 and CdO_6 units. The average Na–Na hopping distance reaches approximately 6.214 Å. Moreover, this one-dimensional diffusion channel appears to be intertwined with PO_4 and CdO_6 polyhedra, significantly differing from the channel observed in the t-$NaFePO_4$ structure, where NaO_6 octahedra are edge-sharing, allowing for a much shorter Na–Na hopping distance of 3.109 Å.[59,60] These structural differences in sodium environments and ion migration distances likely contribute to the distinct sodium insertion/extraction behaviors observed between $NaCdP_3O_9$ and t-$NaFePO_4$. These results confirm that while $NaCdP_3O_9$ does not exhibit the high mobility associated with edge-sharing Na^+ diffusion networks like those in triphylite-type compounds (*e.g.*, $NaFePO_4$), its structural stability and moderate conductivity make it a viable candidate for solid-state sodium-ion conductors in energy storage applications.

3.5. Low-field dielectric response

Examining the dielectric properties of a material offers crucial insights into its polarization behavior, conduction mechanisms, and dielectric relaxation. It is important to note that permittivity is not constant; they fluctuate based on factors such as frequency, temperature, orientation, composition, pressure, and molecular structure. In this study, the real (ε') and

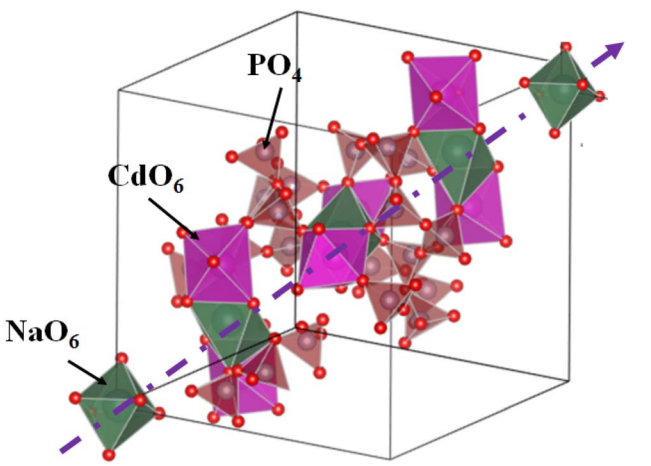

Fig. 8 Sodium-ion diffusion pathway in the $NaCdP_3O_9$ structure along the $[11\bar{1}]$ direction.

imaginary (ε'') components of dielectric permittivity were determined from complex impedance data using the following expressions:

$$\varepsilon^*(\omega) = \varepsilon'(\omega) + j\varepsilon''(\omega) \quad (13)$$

$$\varepsilon' = \frac{Z''}{\omega C_0\left(Z'^2 + Z''^2\right)} \quad (14)$$

$$\varepsilon'' = \frac{Z'}{\omega C_0\left(Z'^2 + Z''^2\right)} \quad (15)$$

The capacitance (C_0) is calculated using the expression ($C_0 = (\varepsilon_0 A)/d$), where ($\varepsilon_0$) denotes the permittivity of free space, (A) represents the electrode surface area, and (d) corresponds to the thickness of the pellet.

The real part (ε') represents the energy stored within the material, while the imaginary part (ε'') quantifies the energy dissipated under the influence of an applied electric field. Fig. 9 (a and b) illustrates the frequency-dependent behavior of (ε') and (ε'') at various temperatures. As shown in Fig. 9(a and b), the dielectric constant is relatively high at low frequencies but gradually decreases as the frequency increases. This behavior is mainly dictated by various polarization mechanisms, including interfacial and dipolar polarization, which collectively impact the material's conduction.[61,62]

Fig. 9(a) illustrates the frequency-dependent variation of the real part of the dielectric permittivity (ε') for the $NaCdP_3O_9$ compound across a temperature range of 473–673 K. A noticeable decrease in ε' with increasing frequency is observed, which can be attributed to the gradual reduction in polarization, as previously discussed. Since dielectric permittivity characterizes a material's ability to become polarized, its behavior is significantly influenced by different polarization mechanisms. At low frequencies (<10^4 Hz) (Region I), interfacial polarization dominates due to charge accumulation at grain boundaries and interfaces. In contrast, at higher frequencies (Region II), dipolar polarization becomes more prominent. However, as frequency increases, the contributions of these polarization mechanisms diminish.[63,64]

Additionally, the real part of the dielectric permittivity, $\varepsilon'(\omega)$, decreases with decreasing temperature, likely due to the reduced mobility and diminished responsiveness of charge carriers at lower temperatures. The real dielectric constant of the investigated sample is approximately 1.19×10^3 at 673 K, indicating a high resistance to electric fields.[65] Furthermore, materials with high dielectric constants are highly desirable for improving the performance of electronic components and low-frequency energy storage devices,[66,67] making $NaCdP_3O_9$ a promising candidate for such applications.

Fig. 9(b) depicts the variation of the imaginary part of the permittivity, $\varepsilon''(\omega)$, as a function of angular frequency over the temperature range of 473 to 673 K. The initial increase in ε'' is attributed to enhanced polarization driven by the thermal energy supplied to the sample.[63] This behavior is consistent

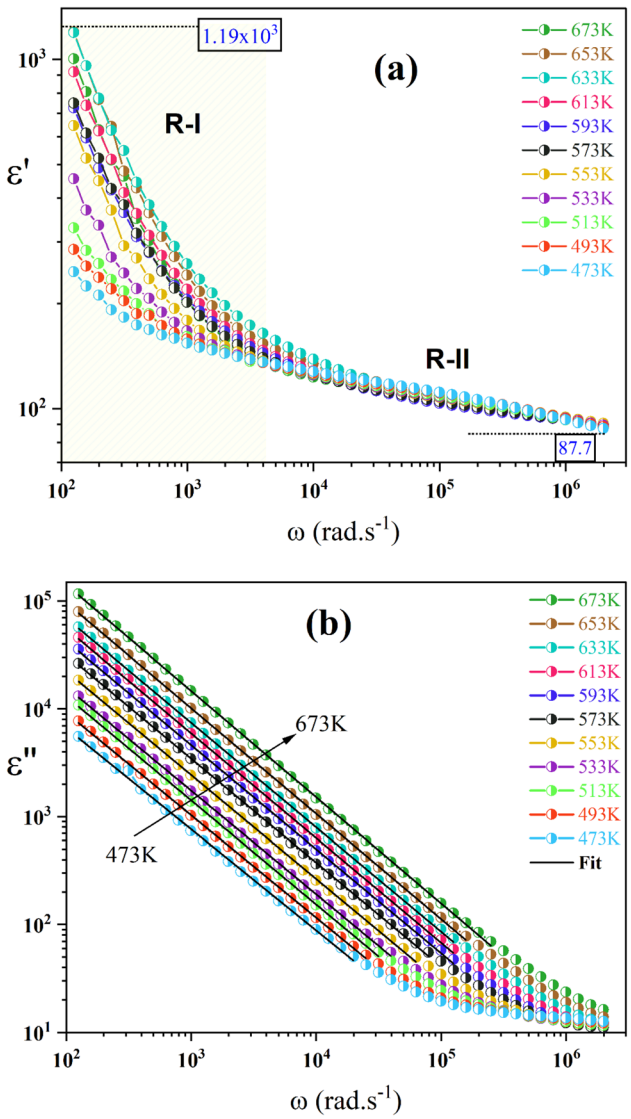

Fig. 9 (a) Evolution of the real part of the permittivity as a function of the angular frequency of the $NaCdP_3O_9$ at various temperatures. (b) Evolution of the imaginary part of the permittivity as a function of the angular frequency of the $NaCdP_3O_9$ at various temperatures.

with the electrodynamic relationship, which predicts a ω^{-1} dependence for dielectric losses.

Notably, while anomalies are evident in the $\varepsilon'(\omega)$ dependence in Fig. 9(a), their presence in $\varepsilon''(\omega)$ is less distinct. However, analyzing relaxation processes in this representation remains challenging due to the significant contribution of DC conductivity, which results in an upward trend in $\varepsilon''(\omega)$ at low frequencies, effectively obscuring relaxation effects.[68,69] Therefore, a more precise evaluation requires differential analysis techniques and an electrical modulus-based approach.

The logarithm of ε'' can be determined using Guitini's theory, as expressed in the following equation:[70]

$$\varepsilon'' = (\varepsilon_s - \varepsilon_\infty)2\pi^2\left(\frac{nq^2}{\varepsilon_0}\right)^3 KT\omega^m\tau_0(W_M)^4 \quad (16)$$

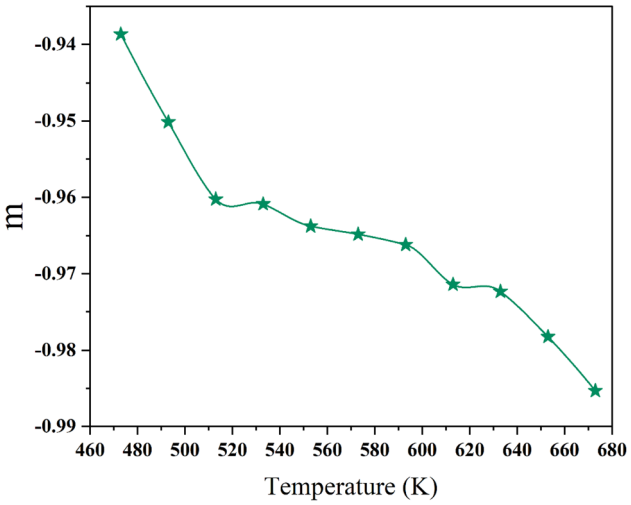

Fig. 10 The temperature dependence of the frequency exponent "m".

In this context, ε_s refers to the dielectric constant at low frequencies, whereas ε_∞ corresponds to the dielectric constant at high frequencies. N represents the state concentration, n is the number of hopping electrons, W_M denotes the barrier height, q is the elementary charge of an electron, and τ_0 signifies the relaxation time.

This law can be rewritten in a simplified form as:[71]

$$\varepsilon'' = C(T)\omega^m \tag{17}$$

In this expression, $C(T)$ denotes a temperature-dependent constant, while m is an exponent that defines the interaction between electric dipoles, as described below:

$$m = -\frac{4K_B T}{W_M} \tag{18}$$

Fig. 10 presents the variation of the parameter "m" with temperature, revealing a direct correlation between the two. As temperature increased within the range of 473–673 K, "m" exhibited a decreasing trend, in agreement with the correlated barrier hopping (CBH) model. These findings are consistent with the electrical properties previously reported for this material.

3.6. Complex modulus formalism

The analysis of the electrical modulus proves to be an effective approach for examining the relaxation process in our sample. The electric modulus (M^*) was determined using the following expression:

$$M' = \frac{\varepsilon'}{\varepsilon'^2 + \varepsilon''^2} \tag{19}$$

$$M'' = \frac{\varepsilon''}{\varepsilon'^2 + \varepsilon''^2} \tag{20}$$

where ε' and ε'' represent the real and imaginary components of the dielectric permittivity, respectively.

Fig. 11(a) illustrates the variation of the real part of the complex modulus (M') for the synthesized $NaCdP_3O_9$ compound as a function of temperature and angular frequency.

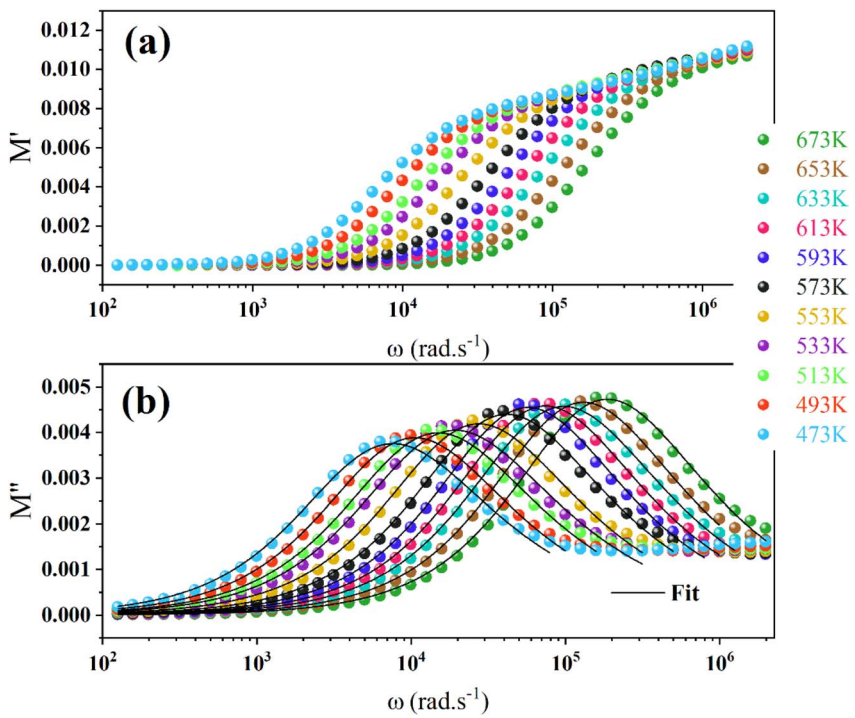

Fig. 11 (a and b) Evolution of the imaginary part of the permittivity as a function of the angular frequency of the $NaCdP_3O_9$ at various temperatures.

At low frequencies, (M') remains close to zero, suggesting minimal or negligible electrode polarization.[72] With increasing frequency, a noticeable dispersion appears, attributed to the localized motion of charge carriers.[73,74] Eventually, (M') stabilizes at asymptotic values, indicating a diminished influence of external electric field forces on charge carrier dynamics.

Fig. 11(b) presents the $M''(\omega)$ plots at various temperatures, revealing no peak in the low-frequency region. However, a broad and well-defined peak emerges at higher frequencies. In the low-frequency range, charge carriers can move freely over long distances, suggesting efficient hopping between neighboring sites.[75] In contrast, at higher frequencies, their movement becomes more restricted. The presence of these peaks provides valuable insights into the transition from long-range to localized charge carrier mobility. As temperature increases, the peaks in M'' shift toward higher frequencies, indicating a thermally activated hopping mechanism. The asymmetric shape of these peaks further highlights the non-Debye nature of the sample's response.[76] To explain this asymmetry, Bergman introduced in 2000 a generalized function based on a modified Kohlrausch–Williams–Watts (KWW) model.[77] This function incorporates two distinct shape parameters to characterize the low- and high-frequency regions, along with a smoothing parameter specifically designed for the M'' spectra. Mathematically, this is expressed as follows:[77]

$$M''(\omega) = \frac{M''_{p}(\omega)}{\left[1-\beta+\left(\frac{\beta}{\beta+1}\right)\left[\beta\left(\frac{\omega_p}{\omega}\right)+\left(\frac{\omega}{\omega_p}\right)^{\beta}\right]\right]} \quad (21)$$

$M''_{p}(\omega)$ represents the peak value of the imaginary part of the modulus M'', while ω_p denotes the characteristic peak frequency. The exponent (β) is a crucial parameter that provides insight into the material's relaxation dynamics. In an ideal dielectric system, where dipole–dipole interactions are minimal (Debye relaxation), (β) equals 1. However, when (β) is less than 1, it indicates pronounced dipole–dipole interactions, characteristic of non-Debye relaxation.[78] The temperature dependence of the parameters obtained from the fitting of eqn (21) is summarized in Table 5.

Table 5 Kohlrausch–Williams–Watts (KWW) law parameters for $NaCdP_3O_9$ at different temperatures

T (K)	M''_{p}	ω_p	β
673	0.00476	157 746.441	0.74080
653	0.00468	125 302.454	0.74590
633	0.00461	99 531.280	0.74941
613	0.00462	79 060.490	0.75218
593	0.00461	49 883.811	0.75661
573	0.00447	39 624.118	0.75925
553	0.00426	25 001.132	0.76120
533	0.00414	19 859.106	0.76219
513	0.00405	12 530.245	0.76453
493	0.00394	9953.128	0.77255
473	0.00380	7906.049	0.77571

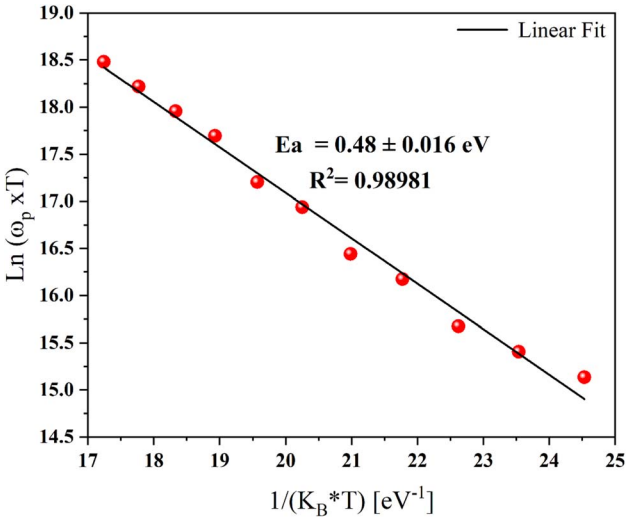

Fig. 12 Evolution of $\ln(\omega_p \times T)$ *versus* the reciprocal of temperature.

The (β) values obtained from the fitting curves were found to be less than unity, confirming the non-Debye relaxation behavior of the compound. Dipole–dipole interactions play a significant role in determining the conductivity of materials, particularly in systems where charge transport occurs through the movement of charged particles or polar molecules. These interactions can influence charge carrier mobility and the overall electrical response of the material in the following manner:[43,79] in materials containing polar molecules or ions with permanent electric dipoles where positive and negative charges are separated by a fixed distance dipole–dipole interactions promote the alignment of these dipoles. When subjected to an external electric field, the dipoles tend to orient themselves along the field direction, resulting in a more ordered internal structure. This alignment facilitates the transport of charge carriers, such as electrons or ions, in preferred directions, thereby enhancing the material's electrical conductivity.

To evaluate the activation energies associated with electrical relaxation phenomena, we extracted the relaxation peak frequencies from the high-frequency peaks centered at (ω_p) in the modulus spectra. Fig. 12 presents the logarithmic variation of ($\omega_p \times T$) as a function of $1/K_B \times T$, revealing that the (ω_p) peak follows the Arrhenius law.

$$\omega_p = \frac{\omega_0}{T}\exp\left(\frac{-E_a}{K_B \times T}\right) \quad (22)$$

where ω_0, E_a, and K_B represent the pre-exponential factor, the activation energy for relaxation, and the Boltzmann constant, respectively. The calculated activation energy was found to be $E_a = 0.48 \pm 0.016$ eV. The obtained values, which closely match those derived from the DC conductivity analysis, indicate a strong correlation between the relaxation dynamics and the charge transport mechanism in the $NaCdP_3O_9$ system.[80]

The combined analysis of Z'' and M'' spectra provides deeper insight into the electrical heterogeneity of the material,[78] as depicted in Fig. 13. The Z'' spectrum features a single peak

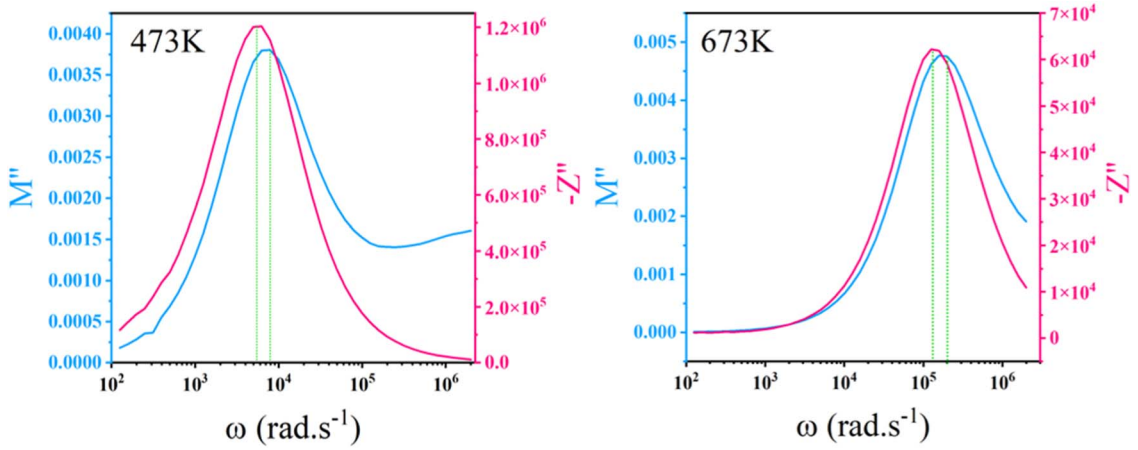

Fig. 13 Combined Z'' and M'' spectroscopic plots.

corresponding to grain boundary contributions, whereas the M'' spectrum displays a non-Debye peak at distinct frequencies. This discrepancy in relaxation peaks suggests spatially confined relaxation dynamics, where localized charge carriers exhibit long-range interactions in the $NaCdP_3O_9$ compound.[81]

4. Conclusion

A thorough investigation of thermally treated $NaCdP_3O_9$ ceramics offers significant insights into their structural, vibrational, optical, and electrical characteristics. This study employs a combination of analytical methods, including X-ray diffraction (XRD), Fourier-transform infrared spectroscopy (FTIR), UV-visible spectroscopy, complex impedance analysis, dielectric measurements, and electric modulus evaluation. XRD analysis confirms that the compound crystallizes in an orthorhombic structure with $P2_12_12_1$ space group symmetry. FTIR spectra verify the characteristic functional groups associated with $NaCdP_3O_9$. UV-vis absorption measurements indicate a direct optical band gap of 3.88 eV, estimated using Tauc's method, suggesting strong potential for optoelectronic applications due to this wide band gap. The material demonstrates favorable optoelectronic behavior, making it an attractive candidate for use in devices requiring wide-gap semiconductors.tg Dielectric studies show significant polarization at low frequencies and high temperatures, pointing to its applicability in energy storage and sensing technologies. Both DC and AC conductivity measurements reveal thermally activated charge transport, with an activation energy of 0.45 eV. The conduction mechanism aligns well with the Correlated Barrier Hopping (CBH) model, indicating effective sodium ion mobility. These findings highlight $NaCdP_3O_9$ as a promising solid electrolyte for sodium-ion-based energy systems, including all-solid-state batteries. The combination of its structural stability, favorable electrical properties, and wide band gap highlights the multifunctional potential of $NaCdP_3O_9$. This study not only enhances the understanding of metaphosphate systems but also underscores their relevance in the development of next-generation, sustainable technologies.

Author contributions

Mayssa Karray: investigation, data curation, formal analysis, visualization, writing – original draft, writing – review & editing. Iheb Garoui: investigation, data curation, formal analysis, visualization, writing – original draft, writing – review & editing. Mehdi Akermi: investigation, data curation, formal analysis, visualization, writing – original draft, writing – review & editing. Ridha Djebali: investigation, formal analysis, visualization, writing – original draft, writing. Abderrazek Oueslati: conceptualization, methodology, formal analysis, validation, writing review & editing. Mohamed Gargouri: supervision, resources, validation, methodology, review & editing.

Conflicts of interest

The authors declare that they have no known competing financial interests or personal relationships that could have appeared to influence the work reported in this paper.

Data availability

The data supporting the findings of this study are available from the corresponding author upon reasonable request.

Acknowledgements

The authors gratefully acknowledge the funding of the Deanship of Graduate Studies and Scientific Research, Jazan University, Saudi Arabia, through Project number: (JU-20250253-DGSSR-ORA-2025).

References

1 S.-H. Kim, G.-I. Shim and S.-Y. Choi, High lithium ion conductivity in mechanically milled Nb-doped m -Li3Fe2(PO4)3, *J. Alloys Compd.*, 2017, **699**, 662–671, DOI: 10.1016/j.jallcom.2016.12.427.

2 C. Zhang, *et al.*, The effect of cobalt promoter on the CO methanation reaction over MoS2 catalyst: a density functional study, *RSC Adv.*, 2017, **7**(20), 11862–11871, DOI: 10.1039/c6ra27422f.

3 Y.-W. Yoo, H.-S. Oh, J.-K. Lee, J.-R. Yoon and S.-H. Lee, Rational Design of Li3V2(PO4)3/C for Phosphate-Based Symmetric Full-Cell Li-Ion Batteries, *Energy Mater. Adv.*, 2024, **5**, 1–11, DOI: 10.34133/energymatadv.0147.

4 B. Babu and A. Balducci, High-Power Sodium-Ion Batteries and Sodium-Ion Capacitors, *Sodium-Ion Batteries*, 2022, 573–601, DOI: 10.1002/9783527825769.ch18.

5 D. Sehrawat, *et al.*, Alkali Metal-Modified P2 NaxMnO2: Crystal Structure and Application in Sodium-Ion Batteries, *Inorg. Chem.*, 2020, **59**(17), 12143–12155, DOI: 10.1021/acs.inorgchem.0c01078.

6 M. G. M. Abdolrasol, S. Ansari, I. A. Sarker, S. K. Tiong and M. A. Hannan, Lithium-ion to sodium-ion batteries transitioning: trends, analysis and innovative technologies prospects in EV application, *Prog. Energy*, 2025, **7**(2), 022007, DOI: 10.1088/2516-1083/adbff0.

7 Q. Yu, *et al.*, Effect of Mn2+ substitution on the dielectric properties of NaMg(PO3)3 ceramics at microwave and terahertz frequencies, *Ceram. Int.*, 2024, **50**(22), 47971–47979, DOI: 10.1016/j.ceramint.2024.09.144.

8 X. Chen, H. Li, P. Zhang and G. Li, Microwave dielectric properties of Co2P2O7 ceramics, *Ceram. Int.*, 2021, **47**(2), 1980–1985, DOI: 10.1016/j.ceramint.2020.09.029.

9 T. Guo, W. Wu, Y. Wang and Y. Li, Relations on synthesis, crystal structure and microwave dielectric properties of SrZnP2O7 ceramics, *Ceram. Int.*, 2012, **38**, S187–S190, DOI: 10.1016/j.ceramint.2011.04.080.

10 Y. Sadin, *et al.*, Novel LiCa(PO3)3 and LiSr(PO3)3 microwave dielectric ceramics, *J. Eur. Ceram. Soc.*, 2024, **44**(3), 1617–1626, DOI: 10.1016/j.jeurceramsoc.2023.10.030.

11 M. Karray, I. Garoui, S. Nasri, S. Znaidia, A. Mahmoud and A. Oueslati, Cesium Iron (III) Pyrophosphate Prepared Using a Solid-State Process: Structure, Mössbauer Spectroscopy, and Relaxation Dynamics, *ChemistrySelect*, 2025, **10**(2), 1–10, DOI: 10.1002/slct.202404727.

12 L. Miladi, M. B. Gzaiel, B. Azaza, A. Oueslati and H. Naïli, Investigation of Morphology, Optical and Electronic Ac Conduction of the Olivine Manganite Compound: NaMnPO4, *Eur. J. Inorg. Chem.*, 2024, **27**(14), 127–138, DOI: 10.1002/ejic.202400038.

13 S. Terny, R. Salgado and M. A. Frechero, Boron oxide addition effect on the microstructure and conductivity of NaZr2(PO4)3 ceramic, *J. Mater. Sci.*, 2024, **60**(1), 367–382, DOI: 10.1007/s10853-024-10551-5.

14 S. Nasri, M. Megdiche and M. Gargouri, AC impedance analysis, equivalent circuit, and modulus behavior of NaFeP2O7 ceramic, *Ionics*, 2014, **21**(1), 67–78, DOI: 10.1007/s11581-014-1147-7.

15 X. Lin, *et al.*, Synthesis, structural, and electrochemical properties of NaCo(PO3)3 cathode for sodium-ion batteries, *J. Solid State Electrochem.*, 2016, **20**(5), 1241–1250, DOI: 10.1007/s10008-015-3114-2.

16 X. Lin, Y. Zhao, Y. Dong and Q. Kuang, Synthesis and structural data of a Fe-base sodium metaphosphate compound, NaFe(PO3)3, *Data Brief*, 2015, **4**, 217–221, DOI: 10.1016/j.dib.2015.05.022.

17 R. V. Lavrik, V. V. Trachevsky and V. A. Diamant, Growth of monocrystals of double polyphosphate NaMn(PO3)3 and its structure, *Catal. Petrochem.*, 2019, **28**, 61–68, DOI: 10.15407/kataliz2019.28.061.

18 C. Zhu, Y. Lu, L. Jiang and Y. Yu, Liquid Crystal Soft Actuators and Robots toward Mixed Reality (Adv. Funct. Mater. 39/2021), *Adv. Funct. Mater.*, 2021, **31**(39), 1–21, DOI: 10.1002/adfm.202170293.

19 M. M. T. Averbuch-Pouchot and A. Durif, Determination des diagrammes d'Equilibre Cd(PO3)2·LiPO3 et Cd(PO3)2·NaPO3; donnees cristallographioues sur CdLi2(PO3)4, CdNa(PO3)3 et CdNa4(PO3)6, *Mater. Res. Bull.*, 1969, **4**(12), 859–867, DOI: 10.1016/0025-5408(69)90041-5.

20 R. Gond, *et al.*, Enabling the Electrochemical Activity in Sodium Iron Metaphosphate [NaFe(PO3)3] Sodium Battery Insertion Material: Structural and Electrochemical Insights, *Inorg. Chem.*, 2017, **56**(10), 5918–5929, DOI: 10.1021/acs.inorgchem.7b00561.

21 J. Faber, EPDIC-8, European Powder Diffraction Conference, *Powder Diffr.*, 2002, **17**(4), 337–338, DOI: 10.1154/1.1536354.

22 E. V. Murashova and N. N. Chudinova, Sodium-manganese cyclopentaphosphate: Synthesis and crystal structure, *Crystallogr. Rep.*, 2000, **45**(4), 568–571, DOI: 10.1134/1.1306563.

23 I. Soudani, K. Ben Brahim, A. Oueslati, H. Slimi, A. Aydi and K. Khirouni, Investigation of structural, morphological, and transport properties of a multifunctional Li-ferrite compound, *RSC Adv.*, 2022, **12**(29), 18697–18708, DOI: 10.1039/d2ra02757g.

24 I. Abrahams, G. E. Hawkes, A. Ahmed, T. Di Cristina, D. Z. Demetriou and G. I. Ivanova, Structures of the chain metaphosphates NaM(PO3)3 (M = Ca or Sr), *Magn. Reson. Chem.*, 2008, **46**(4), 316–322, DOI: 10.1002/mrc.2161.

25 R. Gond, R. P. Rao, V. Pralong, O. I. Lebedev, S. Adams and P. Barpanda, Cubic Sodium Cobalt Metaphosphate [NaCo(PO3)3] as a Cathode Material for Sodium Ion Batteries, *Inorg. Chem.*, 2018, **57**(11), 6324–6332, DOI: 10.1021/acs.inorgchem.8b00291.

26 M. Ferid, N. K. Ariguib and M. Trabelsi, Etude du système KPO3·Sm(PO3)3 et des phases polymorphiques de phosphates condensés KSm(PO3)4, *J. Solid State Chem.*, 1987, **69**(1), 1–9, DOI: 10.1016/0022-4596(87)90002-8.

27 F. Hcini, J. Khelifi and K. Khirouni, Improving of structural, conduction mechanisms, dielectric, optical properties of the sol–gel produced half-doped La0.5Ba0.5CrO3 perovskite for electronics devices, non-linear optical and optoelectronic applications, *Appl. Phys. A: Mater. Sci. Process.*, 2025, **131**(6), 489, DOI: 10.1007/s00339-025-08612-w.

28 A. M. Smith and S. Nie, Semiconductor Nanocrystals: Structure, Properties, and Band Gap Engineering, *Acc. Chem. Res.*, 2009, **43**(2), 190–200, DOI: 10.1021/ar9001069.

29 M. Enneffati, N. K. Maaloul, B. Louati, K. Guidara and K. Khirouni, Synthesis, vibrational and UV–visible studies

of sodium cadmium orthophosphate, *Opt. Quantum Electron.*, 2017, **49**(10), 1–16, DOI: 10.1007/s11082-017-1169-2.

30 J. L. Yuan, *et al.*, VUV spectroscopic properties of Ce3+ and Pr3+-doped AREP2O7-type alkali rare earth diphosphates (A=Na, K, Rb, Cs; RE=Y, Lu), *J. Lumin.*, 2007, **126**(1), 130–134, DOI: 10.1016/j.jlumin.2006.06.002.

31 E. E. N. Madila, *et al.*, Investigation of structural, optical, dielectric, and electrical properties of NaMn4(PO4)3 (NMP) with fillowite-type structure, *J. Mol. Struct.*, 2025, **1322**, 140418, DOI: 10.1016/j.molstruc.2024.140418.

32 O. Taktak, *et al.*, Optical investigations and theoretical simulation of organic-inorganic hybrid: TPA-CoCl4, *Opt. Mater.*, 2024, **150**, 115251, DOI: 10.1016/j.optmat.2024.115251.

33 J. Tauc, Optical Properties of Amorphous Semiconductors, *Amorphous Liq. Semicond.*, 1974, 159–220, DOI: 10.1007/978-1-4615-8705-7_4.

34 S. Ben Yahya, H. El Karout, B. Sahraoui, R. Barillé and B. Louati, Innovative synthesis, structural characteristics, linear and nonlinear optical properties, and optoelectric parameters of newly developed A2ZnGeO4 (A = K, Li) thin films, *RSC Adv.*, 2024, **14**(33), 23802–23815, DOI: 10.1039/d4ra03742a.

35 G. D. Cody, T. Tiedje, B. Abeles, B. Brooks and Y. Goldstein, Disorder and the Optical-Absorption Edge of Hydrogenated Amorphous Silicon, *Phys. Rev. Lett.*, 1981, **47**(20), 1480–1483, DOI: 10.1103/physrevlett.47.1480.

36 T. A. Hameed, S. H. Moustafa, H. Shaban and B. A. Mansour, The effect of selenium on the structural, morphology, optical, electrical properties of Cu2Te thin films for thermoelectric and photovoltaic applications, *Opt. Mater.*, 2020, **109**, 110308, DOI: 10.1016/j.optmat.2020.110308.

37 M. Krimi, F. Hajlaoui, M. S. M. Abdelbaky, S. Garcia-Granda and A. Ben Rhaiem, Investigation of optical, dielectric, and conduction mechanism in lead-free perovskite CsMnBr3, *RSC Adv.*, 2024, **14**(15), 10219–10228, DOI: 10.1039/d4ra01151a.

38 S. Karoui and S. Kamoun, Dielectric study and optical properties of the two-dimensional perovskite (CH3NH3)2Sn(SCN)2Cl2 for optoelectronic applications, *Indian J. Phys.*, 2023, **98**(8), 2731–2744, DOI: 10.1007/s12648-023-03035-w.

39 A. Ghoudi, *et al.*, Optical and electric properties of the organic-inorganic hybrid bis(2-amino-5-picolinium) Tetrachlorocobaltate(II) [(C6H9N2)2CoCl4], *Inorg. Chem. Commun.*, 2024, **168**, 112925, DOI: 10.1016/j.inoche.2024.112925.

40 S. Pujaru, P. Maji, P. Sadhukhan, A. Ray, B. Ghosh and S. Das, Dielectric relaxation and charge conduction mechanism in mechanochemically synthesized methylammonium bismuth iodide, *J. Mater. Sci.: Mater. Electron.*, 2020, **31**(11), 8670–8679, DOI: 10.1007/s10854-020-03402-x.

41 W. H. Shah, *et al.*, Correlated barrier hopping transport and non-Debye type dielectric relaxation in Zn2V2O7 pyrovanadate, *Ceram. Int.*, 2024, **50**(23), 50965–50981, DOI: 10.1016/j.ceramint.2024.10.008.

42 I. Garoui, N. Ben Hamadi, S. Nasri, A. Oueslati, A. Guesmi, L. Khezami and H. Naïli, Dielectric relaxation and electrothermal charge carrier transport via correlated barrier hopping in the solid electrolyte TlFeP2O7: Experimental and theoretical modeling, *Ceram. Int.*, 2025, **51**(19), 29510–29525, DOI: 10.1016/j.ceramint.2025.04.155.

43 M. ben gzaiel, I. Garoui, F. N. Almutairi, I. Mbarek and O. A, Lead-Free halide perovskites for optoelectronic application: Investigation of structural, optical, electric and dielectric behaviors, *Opt. Mater.*, 2024, **154**, 115664, DOI: 10.1016/j.optmat.2024.115664.

44 S. Karmakar, S. Varma and D. Behera, Investigation of structural and electrical transport properties of nano-flower shaped NiCo2O4 supercapacitor electrode materials, *J. Alloys Compd.*, 2018, **757**, 49–59, DOI: 10.1016/j.jallcom.2018.05.056.

45 W. Chen, W. Zhu, O. K. Tan and X. F. Chen, Frequency and temperature dependent impedance spectroscopy of cobalt ferrite composite thick films, *J. Appl. Phys.*, 2010, **108**(3), 034101, DOI: 10.1063/1.3457217.

46 S. Brahma, R. N. P. Choudhary and A. K. Thakur, AC impedance analysis of LaLiMo2O8 electroceramics, *Phys. B*, 2005, **355**(1–4), 188–201, DOI: 10.1016/j.physb.2004.10.091.

47 C. Bharti and T. P. Sinha, Structural and ac electrical properties of a newly synthesized single phase rare earth double perovskite oxide: Ba2CeNbO6, *Phys. B*, 2011, **406**(9), 1827–1832, DOI: 10.1016/j.physb.2011.02.038.

48 S. B. Yahya and B. Louati, Characterization of the structure and conduction behavior of overlapping polaron tunnel of dipotassium zinc orthogermanate, *J. Alloys Compd.*, 2021, **876**, 159972, DOI: 10.1016/j.jallcom.2021.159972.

49 A. K. Jonscher, The 'universal' dielectric response, *Nature*, 1977, **267**(5613), 673–679, DOI: 10.1038/267673a0.

50 B. Louati, F. Hlel and K. Guidara, Ac electrical properties and dielectric relaxation of the new mixed crystal (Na0.8Ag0.2)2PbP2O7, *J. Alloys Compd.*, 2009, **486**(1–2), 299–303, DOI: 10.1016/j.jallcom.2009.06.148.

51 I. Garoui, *et al.*, New organic–inorganic chloride (2-amino-4-methylpyridinium hexachlorostannate): Crystal structure, BFDH morphology, and electrical conduction mechanism, *J. Phys. Chem. Solids*, 2025, **206**, 112840, DOI: 10.1016/j.jpcs.2025.112840.

52 R. Mendil, S. Nasri and A. Oueslati, Structural investigation, vibrational study, and Na-ion transport properties of NaGaP2O7 as sodium solid electrolyte, *Ionics*, 2025, **31**(3), 2501–2514, DOI: 10.1007/s11581-025-06087-6.

53 I. Ben Slima, K. Karoui, K. Khirouni, A. Mahmoud, F. Boschini and A. Ben Rhaiem, Investigation of the optical and dielectric properties of NaCu0.2Fe0.8-xMnxO2 (x = 0.4; 0.5; 0.6; 0.7) layered oxide materials, *Inorg. Chem. Commun.*, 2023, **157**, 111444, DOI: 10.1016/j.inoche.2023.111444.

54 S. Ben Yahya, I. Garoui, M. Zaghrioui, A. Oueslati and B. Louati, Solid-state synthesized Li4GeO4 germanate: an exploration of its structure, vibrational characteristics,

electrical conductivity, and dielectric properties, *RSC Adv.*, 2025, **15**(12), 9295–9304, DOI: 10.1039/d5ra01165e.

55 A. A. A. Qahtan, S. Husain, A. Somvanshi, W. Khan and Y. K. Manea, Influence of Mn doping on dielectric properties, conduction mechanism and photocatalytic nature of gadolinium-based orthochromites, *J. Mater. Sci.: Mater. Electron.*, 2020, **31**(12), 9335–9351, DOI: 10.1007/s10854-020-03474-9.

56 M. Rani, R. C. Pawar and N. Panwar, Exploring the comparison of optical, dielectric and photocatalytic performance of Yb3+ and Gd3+ half-doped DyCrO3 nanostructures, *Mater. Chem. Phys.*, 2024, **314**, 128848, DOI: 10.1016/j.matchemphys.2023.128848.

57 S.-Y. Jun, D. Jung, J.-Y. Kim and S. Yu, Dielectric characteristics of graphene-encapsulated barium titanate polymer composites, *Mater. Chem. Phys.*, 2020, **255**, 123533, DOI: 10.1016/j.matchemphys.2020.123533.

58 Y. Ben Taher, A. Oueslati, N. K. Maaloul, K. Khirouni and M. Gargouri, Conductivity study and correlated barrier hopping (CBH) conduction mechanism in diphosphate compound, *Appl. Phys. A: Mater. Sci. Process.*, 2015, **120**(4), 1537–1543, DOI: 10.1007/s00339-015-9353-3.

59 P. Moreau, D. Guyomard, J. Gaubicher and F. Boucher, Structure and Stability of Sodium Intercalated Phases in Olivine FePO4, *Chem. Mater.*, 2010, **22**(14), 4126–4128, DOI: 10.1021/cm101377h.

60 R. Tripathi, S. M. Wood, M. S. Islam and L. F. Nazar, Na-ion mobility in layered Na2FePO4F and olivine Na[Fe,Mn]PO4, *Energy Environ. Sci.*, 2013, **6**(8), 2257, DOI: 10.1039/c3ee40914g.

61 H. Dhahri, *et al.*, Advanced characterization of the structural and electrical properties of La0.6Ce0.2Ba0.2FeO3 synthesized via the sol–gel method, *J. Korean Phys. Soc.*, 2025, 201–212, DOI: 10.1007/s40042-025-01402-w.

62 Y. Moualhi, M. Smari, H. Nasri and H. Rahmouni, Combined transport and dielectric models and experimental characterization based on impedance spectroscopy for studying the microstructural and transport properties of electro-ceramic perovskites, *Mater. Today Commun.*, 2024, **38**, 108529, DOI: 10.1016/j.mtcomm.2024.108529.

63 M. C. Dimri, A. Verma, S. C. Kashyap, D. C. Dube, O. P. Thakur and C. Prakash, Structural, dielectric and magnetic properties of NiCuZn ferrite grown by citrate precursor method, *Mater. Sci. Eng., B*, 2006, **133**(1–3), 42–48, DOI: 10.1016/j.mseb.2006.04.043.

64 K. Guettiti, *et al.*, The study of structural, dielectric, impedance and modulus properties of La0·8Pb0·2FeO3 doped by 25% Mg into the B-site, *Phys. B*, 2023, **655**, 414771, DOI: 10.1016/j.physb.2023.414771.

65 I. Garoui, M. Mallek, F. N. Almutairi, W. Rekik and A. Oueslati, Synthesis, Structural characterization and complex impedance analysis of a novel organic-inorganic hybrid compound based on Mercury (II) chloride, *J. Mol. Struct.*, 2024, **1315**, 138881, DOI: 10.1016/j.molstruc.2024.138881.

66 K. Akhrib, I. Gharbi, M. Sassi, M. Tliha, M. Ben Gzaiel and A. Oueslati, Electrical transport and dielectric relaxation mechanisms in AgCrP2O7: Synthesis and characterization, *J. Mol. Struct.*, 2025, **1333**, 141727, DOI: 10.1016/j.molstruc.2025.141727.

67 I. Ouni, Y. Moualhi and H. Rahmouni, Thermistor and capacitor parameter analysis through electrical and dielectric investigations of manganite systems for technological applications, *Sens. Actuators, A*, 2025, **384**, 116300, DOI: 10.1016/j.sna.2025.116300.

68 A. Molak, M. Paluch, S. Pawlus, Z. Ujma, M. Pawełczyk and I. Gruszka, Properties of (Bi1/9Na2/3)(Mn1/3Nb2/3) O3analysed within dielectric permittivity, conductivity, electric modulus and derivative techniques approach, *Phase Transitions*, 2006, **79**(6–7), 447–460, DOI: 10.1080/01411590600892336.

69 S. Pawlus, S. Hensel-Bielowka, K. Grzybowska, J. Zioło and M. Paluch, Temperature behavior of secondary relaxation dynamics in tripropylene glycol, *Phys. Rev. B: Condens. Matter Mater. Phys.*, 2005, **71**(17), 174107, DOI: 10.1103/physrevb.71.174107.

70 J. C. Giuntini, J. V. Zanchetta, D. Jullien, R. Eholie and P. Houenou, Temperature dependence of dielectric losses in chalcogenide glasses, *J. Non-Cryst. Solids*, 1981, **45**(1), 57–62, DOI: 10.1016/0022-3093(81)90089-2.

71 K. M. Batoo, S. Kumar, C. G. Lee and A. Alimuddin, Study of dielectric and ac impedance properties of Ti doped Mn ferrites, *Curr. Appl. Phys.*, 2009, **9**(6), 1397–1406, DOI: 10.1016/j.cap.2009.03.012.

72 F. S. Howell, R. A. Bose, P. B. Macedo and C. T. Moynihan, Electrical relaxation in a glass-forming molten salt, *J. Phys. Chem.*, 1974, **78**(6), 639–648, DOI: 10.1021/j100599a016.

73 K. L. Ngai and C. León, Recent advances in relating macroscopic electrical relaxation data to microscopic movements of the ions in ionically conducting materials, *Solid State Ionics*, 1999, **125**(1–4), 81–90, DOI: 10.1016/s0167-2738(99)00161-7.

74 S. Sasaki, C. T. Prewitt, J. D. Bass and W. A. Schulze, Orthorhombic perovskite CaTiO3 and CdTiO3: structure and space group, *Acta Crystallogr., Sect. C: Cryst. Struct. Commun.*, 1987, **43**(9), 1668–1674, DOI: 10.1107/s0108270187090620.

75 S. Nasri, A. Jraba, I. Garoui, A. Oueslati and E. Elaloui, Potassium tin chloride (K2SnCl6) as a lead-free perovskite: anti-solvent synthesis, structural characterization, and charge transport properties, *RSC Adv.*, 2025, **15**(7), 5369–5380, DOI: 10.1039/d5ra00090d.

76 S. Chkoundali, I. Garoui, W. Trigui and A. Oueslati, Crystal structure, Hirshfeld surface analysis, conduction mechanism and electrical modulus study of the new organic–inorganic compound [C8H10NO]2HgBr4, *RSC Adv.*, 2024, **14**(13), 8971–8980, DOI: 10.1039/d4ra00689e.

77 R. Cheruku, L. Vijayan and G. Govindaraj, Electrical relaxation studies of solution combustion synthesized nanocrystalline Li2NiZrO4 material, *Mater. Sci. Eng., B*, 2012, **177**(11), 771–779, DOI: 10.1016/j.mseb.2012.04.005.

78 M. Ram, Structure and electrical conduction behavior of LiZnVO4 ceramic prepared by solution-based chemical route, *J. Alloys Compd.*, 2011, **509**(18), 5688–5691, DOI: **10.1016/j.jallcom.2011.02.128**.

79 H. Elgahami, *et al.*, Mercury (II) compound with a quaternary phosphonium: X-ray structure, Hirshfeld surface analysis, optical band gap, and dielectric properties, *Ionics*, 2024, **31**(1), 1095–1110, DOI: **10.1007/s11581-024-05944-0**.

80 Y. Wang, *et al.*, Microstructure and electrical properties of Nb-doped SrTiO3-BiFeO3 based lead-free ceramics, *J. Am. Ceram. Soc.*, 2021, **105**(3), 2020–2028, DOI: **10.1111/jace.18194**.

81 M. Mallek, I. Garoui, F. N. Almutairi, I. Chaabane, W. Rekik and A. Oueslati, Synthesis, structural characterization, Hirshfeld surface analysis, and electrical properties of a zinc (II)-based organic–inorganic hybrid compound, *J. Mater. Sci.: Mater. Electron.*, 2025, **36**(8), 458, DOI: **10.1007/s10854-025-14480-0**.